Int. J. Heat Mass Transfer, Vol. 24, No. 12, pp. 1959–1970, 1981.
Printed in Great Britain

0017-9310/81/121959-12 $02.00/0
© 1981 Pergamon Press Ltd.

AN INVESTIGATION OF A LAMINAR DIFFUSION FLAME ADJACENT TO A VERTICAL FLAT PLATE BURNER

K. VINCENT LIU,* JOHN R. LLOYD and K. T. YANG
Department of Aerospace and Mechanical Engineering, University of Notre Dame, Notre Dame, IN 46556, U.S.A.

(*Received* 22 *September* 1981 *and in revised form* 5 *June* 1981)

Abstract—An analytical and experimental study of a methane diffusion flame in the region adjacent to a vertical flat burner is made. The appropriate boundary layer equations including one-dimensional non-gray non-homogeneous thermal radiation formulated on the basis of the exponential wide-band model are solved by the local non-similarity method to yield the gas species, laminar velocity and temperature profiles inside the diffusion flame boundary layer. It is demonstrated that variable physical properties of the gas mixture have important effects on the flame temperature and structure. The diffusion flame shape and temperature distribution in the boundary layer have also been measured by a Mach–Zehnder interferometer to verify the theoretical results. The peak flame temperature, its location and the temperature profile inside the flame sheet are accurately predicted with the two-equation solutions which, however, underestimate the boundary layer thicknesses. Based on these results, the feasibility of a gray gas radiation model is also explored.

NOMENCLATURE

$A_{i,j}$, total band absorptance of ith gas band of the jth species [1/cm];
B, $= v_w k_w^{1/2} N_R^{1/2}/v_w$;
c, $= (g/4v_w^2)^{1/4}$;
c_p, specific heat of the gas mixture [cal/gm K];
$\bar{c}_p$, local mean specific heat of the gas mixture, defined as $\int_{T_\infty}^{T} c_p \, dT/(T - T_\infty)$;
$\tilde{\bar{c}}_p$, defined as $\bar{c}_p/c_{p_\infty}$;
D, mass diffusion coefficient [cm²/s];
f, non-dimensional stream function;
g, defined as $df/d\xi$, or acceleration of gravity [cm/s²];
g_c, Newton's gravity constant [gm-cm/g-s²];
h, enthalpy of gas mixture [cal/gm-mol];
$\hat{h}$, defined as h/Q;
k, thermal conductivity of gas mixture [cal/s-cm-K];
L, physical length [cm];
Le, $= k/c_p D$, Lewis number;
$\dot{m}'''_\alpha$, volumetric generation rate of species α [gm/s-cm³];
m_α, molecular weight of species α [gm/gm-mol];
$\dot{M}$, volumetric fuel consumption rate [gm-mol/s-cm³];
N, radiation constant, defined as $X_0/\sigma T_f^3$ [cm³-s-K/cal];
P, pressure [atm];
Pr, $= \nu/\alpha$, Prandtl number;
q''_r, total radiation heat flux [cal/s-cm²];
Q, heat of combustion [cal/gm-mol];
$\dot{Q}'''$, volumetric heat generation rate [cal/s-cm³];
R, gas constant of gas mixture [cal/gm-K];
S_c, $= \nu/D$, Schmidt number;
V_α, defined as $dW_\alpha/d\xi$;
T, absolute temperature [K];
$\bar{T}$, defined as $1/(y - y') \int_{y'}^{y} T(y'')\, dy''$;
T_f, theoretical flame temperature [K];
u, v, velocity components of gas mixture in x, y direction, respectively [cm/s];
W_α, defined as $(\hat{Y}_\alpha - \hat{Y}_0 + \hat{Y}_{0,\infty})\, Q/h_\infty$;
x, y, coordinates [cm];
X_0, characteristic length [cm];
Y_α, mass concentration of species α;
$\hat{Y}_\alpha$, defined as $Y_\alpha/M_\alpha\,(\nu''_\alpha - \nu'_\alpha)$.

Greek symbols

α, integrated band intensity [1/atm-cm²]
β, a weighting factor;
ρ, density of gas mixture [gm/cm³];
ψ, stream function [cm²/s];
σ, Stephen–Boltzman constant [cal/s-cm²-K⁴];
$\Gamma_{i,j}$, transmittance of ith gas and jth species;
ν''_α, stoichiometric coefficient of product $\alpha[0]$;
ν''_α, stoichiometric coefficient of reactants $\alpha[0]$;
μ, dynamic viscosity [gm/s-cm];
η, transformed y coordinate [0];
ξ, transformed x coordinate [0];
ρ_α, density of gas species α [gm/cm³];
$\omega_{i,j}$ band width parameter of ith gas band and jth gas species [1/cm];

*Present address: Shell Development Co., Houston, Texas.

θ, defined as $h/h_\infty - (\hat{Y}_0 - \hat{Y}_{0,\infty})Q/h_\infty$ [0];
ϕ, defined as $d\theta/d\xi$;
τ_H, optical thickness [0];
κ, extinction coefficient of radiation [1/cm];
κ_p, mean Planck absorption coefficient [1/cm].

Subscripts

∞, refers to the quantity at ambient condition;
c, carbon property;
H, hydrogen property;
F, fuel property;
o, oxidizer property;
P, product property;
w, refers to wall condition;
ξ, differentiation with respect to;
x, y, components in x and y directions.

INTRODUCTION

IN RECENT years, the interaction of thermal radiation with other modes of heat transfer has attracted considerable attention. It has been demonstrated that gas radiation has a significant effect on the rate of heat transfer in free convection [1]. In the studies by Novotny *et al.* [2–4] and Audunson and Gebhart [5], it was pointed out that the gray gas approximation does not give satisfactory accuracy. The exponential wide-band gas radiation model of Edwards and Menard [6], however, has led to good results in the calculation of total band absorptance for real gases under moderate pressure conditions. In boundary layer flows involving such complications as a diffusion flame with sharp temperature gradients and non-homogeneous components in the absorbing–emitting gas mixture, thermal radiation affects not only the temperature field, but also the fuel consumption rate on the surface. Due to the complexity of this phenomenon, however, the radiation effect has been either ignored [7, 8] or estimated by a simple non-predictive approach [9] by the various researchers.

The present study analytically and experimentally examines the interaction of radiation and free convection within the boundary layer created by a diffusion flame along a vertical flat plate. The absorbing–emitting combustion gases are treated as non-gray and non-homogeneous. Their gas band absorptance is calculated with the use of the exponential wide-band model [6, 10] and the scaling approximation for radiation parameters [11, 12]. A similar approach was used by Negrelli, Lloyd and Novotny [13] in an analytical and experimental study of radiation-free convection interaction for a methane–air diffusion flame at the lower stagnation region of a horizontal cylinder. For the specific geometry considered, the combustion radiation problem was solvable by a similarity solution.

In the present non-similar problem, the governing equations are treated by the now well known local non-similarity method of Sparrow [14]. In the corresponding experimental study, the temperature distributions in a methane diffusion flame along a porous vertical plate are measured by a Mach–Zehnder interferometer, and compared with the theoretical results.

MATHEMATICAL FORMULATIONS

A schematic diagram of the diffusion flame considered herein is shown in Fig. 1. The origin of the coordinate system is at the bottom edge of the porous plate. After the gas fuel is injected from the back of the plate and ignited, the flame develops on the front of the plate, and the 2-dim. velocity and enthalpy fields are described by the following laminar boundary layer conservation equations for steady compressible flows:

$$\frac{\partial}{\partial x}(\rho u) + \frac{\partial}{\partial y}(\rho v) = 0, \tag{1}$$

$$\rho u\frac{\partial u}{\partial x} + \rho v\frac{\partial u}{\partial y} = \frac{\partial}{\partial y}\left(\mu\frac{\partial u}{\partial y}\right) + g(\rho_\infty - \rho), \tag{2}$$

$$\rho u\frac{\partial h}{\partial x} + \rho v\frac{\partial h}{\partial y} = \frac{\partial}{\partial y}\left(\frac{k}{c_p}\frac{\partial h}{\partial y}\right) - \frac{dq_r''}{dy} + \dot{Q}'''. \tag{3}$$

Here the enthalpy is defined by

$$h = \int_{T_\infty}^{T} c_p dT$$

and the q_r'' denotes the thermal radiative flux in the y direction. In the combustion process of gaseous methane, the gas mixture is composed of the fuel, the oxidizer, and the products of combustion. Five gas species are considered in this study, namely: methane (CH_4), oxygen (O_2), water vapor (H_2O), carbon dioxide (CO_2) and nitrogen (N_2). Any intermediate combustion species are ignored [13]. The usual assumption of infinite reaction rates in the methane diffusion flame is also employed here. The chemical reaction equation can be expressed as

$$\nu_F'(CH_4) + \nu_o'(O_2) + \nu_p'(H_2O + CO_2) \rightarrow \nu_F''(CH_4) + \nu_o''(O_2) + \nu_P''(H_2O + CO_2) + Q.$$

According to the stoichiometric condition, the molecular coefficients are given by

$$\nu_F' = 1, \quad \nu_o' = 2, \quad \nu_p' = 0;$$
$$\nu_F'' = 0, \quad \nu_o'' = 0, \quad \nu_P'' = \nu_c'' + \nu_H'' = 1 + 2 = 3.$$

Inside the diffusion flame the mass conservation equations for the species are written as:

$$\rho u\frac{\partial Y_F}{\partial x} + \rho v\frac{\partial Y_F}{\partial y} = \frac{\partial}{\partial y}\left(\rho D\frac{\partial Y_F}{\partial y}\right) + \dot{m}_F''', \tag{4}$$

$$\rho u\frac{\partial Y_o}{\partial x} + \rho v\frac{\partial Y_o}{\partial y} = \frac{\partial}{\partial y}\left(\rho D\frac{\partial Y_o}{\partial y}\right) + \dot{m}_o''', \tag{5}$$

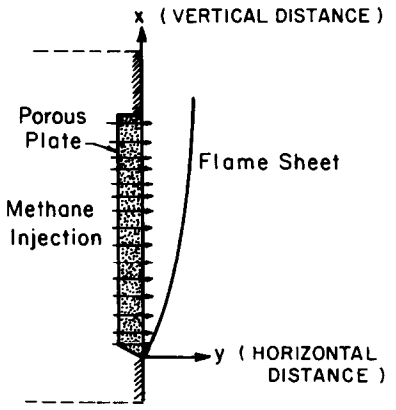

FIG. 1. Schematic drawing of methane flame adjacent to a vertical porous surface.

$$\rho u\frac{\partial Y_P}{\partial x}+\rho v\frac{\partial Y_P}{\partial y}=\frac{\partial}{\partial y}\left(\rho D\frac{\partial Y_P}{\partial y}\right)+\dot{m}'''_P, \quad (6)$$

where $Y_P = Y_c + Y_H = 1 - Y_N - Y_o - Y_F$.
Also, the species mass production and heat generation quantities are interrelated as follows:

$$\frac{\dot{m}'''_F}{M_F(v''_F-v'_F)}=\frac{\dot{m}'''_o}{M_o(v''-v'_o)}=\frac{\dot{m}'''_P}{M_P(v''_P-v'_P)}=\frac{\dot{Q}'''}{Q}. \quad (7)$$

Finally, under the assumption of an ideal gas under 1 atm pressure, the equation of state is simply given by: ρT = constant. In this problem the thermal radiation term in the energy equation depends only on y and the injection rate of methane through the surface is taken to be uniform. Consequently a similarity solution does not exist. The local non-similarity method [14] is utilized here to solve the governing equations. The species and energy equations are first combined to reduce the number of the partial differential equations and to eliminate the source terms. In species equations (4)–(6), the mass generation rate $\dot{m}'''_\alpha$ and the oxygen species equation (5) can be made to cancel out by introducing dimensionless species concentration parameters W_α:

$$W_\alpha=(\hat{Y}_\alpha-\hat{Y}_o+\hat{Y}_{o,\infty})\frac{Q}{h_\infty}, \quad \alpha = F, o, P,$$

and combining equations (4)–(6) along with equation (7). The resulting species equations may then be written as

$$\rho u\frac{\partial W_F}{\partial x}+\rho v\frac{\partial W_F}{\partial y}=\frac{\partial}{\partial y}\left(\rho D\frac{\partial W_F}{\partial y}\right), \quad (8)$$

$$\rho u\frac{\partial W_P}{\partial x}+\rho v\frac{\partial W_P}{\partial y}=\frac{\partial}{\partial y}\left(\rho D\frac{\partial W_P}{\partial y}\right). \quad (9)$$

Similarly, the heat generation rate $\dot{Q}'''$ can be eliminated by introducing an energy parameter defined by

$$\theta = h/h_\infty - (\hat{Y}_o - \hat{Y}_{o,\infty})\,Q/h_\infty,$$

and the energy equation then becomes, with the assumption of $Pr = Sc$,

$$\rho u\frac{\partial\theta}{\partial x}+\rho v\frac{\partial\theta}{\partial y}=\frac{\partial}{\partial y}\left(\frac{k}{c_p}\frac{\partial\theta}{\partial y}\right)-\frac{1}{h_\infty}\frac{dq''_r}{dy}. \quad (10)$$

The coupled governing equations (1), (2), (8)–(10) are further transformed into a new coordinate system (ξ, η) defined by

$$\xi=\frac{x^{1/2}}{C^2k_w}\left(\frac{1}{N_R}\right), \eta = Cx^{-1/4}\int_0^y\frac{\rho}{\rho_w}dy,$$

where $C = (g/4\nu_w^2)^{1/4}$ and $N = X_o/\sigma T_f^3$. It is seen that ξ is a streamwise variable associated wtih thermal radiation, and η is the psuedo-similarity variable. Now similar to the vertical plate free convective problem, a stream function ψ is introduced to eliminate the velocity components. This in turn is eliminated by the formulation of a dimensionless stream function f defined by

$$\psi = 4C\nu_w\,x^{3/4}\,f(\xi,\eta).$$

In addition to the perfect gas law, it is also assumed that $\rho\mu$ = constant and $\rho k/c_p$ = constant, which are commonly utilized in compressible boundary layer analysis [7, 13]. Furthermore, a flame sheet model is invoked here, which stipulates that no oxygen exists between the fuel surface and the flame sheet, and that the concentration of the gas fuel vanishes beyond the flame sheet, i.e.

$0\le\eta\le\eta_f$, $\hat{Y}_o = 0$ or

$$\frac{T}{T_\infty}=\left[\theta-\hat{Y}_{o,\infty}\frac{Q}{h_\infty}\right]\frac{1}{\bar{c}_p}+1;$$

$\eta>\eta_f$, $\hat{Y}_F = 0$ or

$$\frac{T}{T_\infty}=y[\theta-W_F]\frac{1}{\bar{c}_p}+1.$$

Now the transformed governing equations in the (ξ,η) coordinate system can be readily derived, resulting in

$$\frac{1}{Sc}W''_F+3fW'_F=2\xi[f'(W_F)_\xi-f_\xi(W'_F)], \quad (11)$$

$$\frac{1}{Sc}W''_P+3fW'_P=2\xi[f'(W_P)_\xi-f_\xi(W'_P)]. \quad (12)$$

For $0\le\eta\le\eta_f$,

$$f'''-2(f')^2+3ff''+\left[\theta-\hat{Y}_{o,\infty}\frac{Q}{h_\infty}\right]\frac{1}{\bar{c}_p}=2\xi[f'_\xi f'-f''f_\xi], \quad (13)$$

$$\frac{1}{Pr}\theta''+3f\theta'-\frac{1}{Pr}(\xi N)\left(\frac{c_{p_w}}{c_{p_\infty}}\right)\left(\frac{\rho_w}{\rho}\right)\left[\theta-\hat{Y}_{o,\infty}\frac{Q}{h_\infty}\right]\times\frac{1}{\bar{c}_pT_\infty}\frac{dq''_r}{dy}=2\xi[f'\theta_\xi-f_\xi\theta'], \quad (14)$$

$$f'''-2(f')^2+3ff''-\frac{1}{\bar{c}_p}[\theta-W_F]=2\xi[f'_\xi f'-f''f_\xi], \quad (15)$$

$$\frac{1}{Pr}\theta''+3f\theta'-\frac{1}{Pr}(\xi N)\left(\frac{c_{p_w}}{c_{p_\infty}}\right)\left(\frac{\rho_w}{\rho}\right)\frac{1}{\tilde{c}_p}[\theta-W_F]\times\frac{1}{T_\infty}\frac{dq_r''}{dy}=2\xi[f'\theta_\xi-f_\xi\theta']. \quad (16)$$

The prime and the subscript ξ denote $\partial/\partial\eta$ and $\partial/\partial\xi$, respectively. The physical boundary conditions are:

$y=0$, $u=0$, $v=v_w$ (constant), $h=h_w$, $Y_o=0$, $Y_F=(Y_F)_w$, $Y_P=(Y_P)_w$;

$y\to\infty$, $u\to 0$, $h\to h_\infty$, $Y_o=Y_{o,\infty}$, $Y_F=Y_P=0$.

When transformed, they reduce to:

for $\eta=0$,

$$f_w=-\left[\frac{v_w k_w^{1/2}}{3\nu_w}(3N)^{1/2}+\frac{2}{3}\xi f_\xi|_{\eta=0}\right]f'=0,$$

$$(W_F)_w=\frac{-W_f'(\xi,0)}{Sc[3f_w+2\xi f_\xi|_{\eta=0}]}+\frac{Q}{h_\infty M_f(v_F''-v_F')}+\hat{Y}_{o,\infty}\frac{Q}{h_\infty},$$

$$(W_P)_w=\frac{-W_P'(\xi,0)}{Sc[3f_w+2\xi f_\xi|_{\eta=0}]}+\hat{Y}_{o,\infty}\frac{Q}{h_\infty},$$

$$\theta_w=\frac{h_w}{h_\infty}+\hat{Y}_{o,\infty}\frac{Q}{h_\infty};$$

and for $\eta\to\infty$,

$$f'=W_F=W_P=\theta\to 0$$

where v_w and h_w are determined from experiments.

LOCAL SIMILARITY SOLUTION

The 1st-order approximation in the local non-similarity solution is the local similarity solution. All the ξ-derivatives in the right-hand side of equations (11)–(16) are considered negligible and are thus deleted. Accordingly, the ξ-derivatives in the boundary conditions can also be dropped. Therefore, the remaining equations can be solved as coupled ordinary differential equations at any specified streamwise location ξ. It is interesting to point out that equations (11) and (12) have the same solutions if both variables W_F and W_P are normalized by their boundary condition $(W_F)_w$ and $(W_P)_w$, respectively.

THE TWO-EQUATION MODEL

In accordance with the local non-similarity scheme [14], the 2nd-order approximation is achieved by obtaining approximate values for the deleted ξ-derivatives in the local similarity solution. Let

$$g(\xi,\eta)=\frac{\partial f}{\partial\xi},\ V_\infty(\xi,\eta)=\frac{\partial W_\infty}{\partial\xi},\ \phi(\xi,\eta)=\frac{\partial\theta}{\partial\xi}.$$

After replacing the terms in the right-hand side of equations (11)–(16), the governing equations are then differentiated with respect to ξ. The 2nd-order derivatives of ξ in the new equations, such as

$$\xi\frac{d}{d\xi}[f'V_\infty-g(W_\infty)'],\quad \xi\frac{d}{d\xi}[f'\phi-g\theta']$$

and $\xi\dfrac{d}{d\xi}[f'g'-gf'']$

are neglected, resulting in another set of ordinary differential equations with ξ serving as a parameter. The boundary conditions are then treated similarly. Finally these new equations, combined with the original equations (11)–(16) form the governing ordinary differential equations in the two-equation model. They are written as follows:

$$\frac{1}{Sc}W_F''+3fW_F'-2\xi(f'V_F-gW_F')=0, \quad (17)$$

$$\frac{1}{Sc}V_F''+5gW_F'+3fV_F'-2f'V_F=0, \quad (18)$$

$$\frac{1}{Sc}W_P''+3fW_P'-2\xi(f'V_P-gW_P')=0, \quad (19)$$

$$\frac{1}{Sc}V_P''+5gW_P'+3fV_P'-2f'V_P=0. \quad (20)$$

For $0\le\eta\le\eta_f$,

$$f'''-2(f')^2+3ff''+\frac{1}{\tilde{c}_p}\left[\theta-\hat{Y}_{o,\infty}\frac{Q}{h_\infty}\right]-2\xi(fg'-gf'')=0, \quad (21)$$

$$g'''+5gf''+3fg''-6f'g'+\frac{\phi}{\tilde{c}_p}+\theta\frac{d}{d\xi}\left(\frac{1}{\tilde{c}_p}\right)=0, \quad (22)$$

$$\frac{1}{Pr}\theta''+3f\theta'-\frac{1}{Pr}(\xi N)\left(\frac{c_{p_w}}{c_{p_\infty}}\frac{\rho_w}{\rho_\infty}\right)\frac{1}{\tilde{c}_p}\times\left[\theta-\hat{Y}_{o,\infty}\frac{Q}{h_\infty}\right]\frac{1}{T_\infty}\frac{dq_r''}{dy}-2\xi(f'\phi-g\theta')=0, \quad (23)$$

$$\frac{1}{Pr}\phi''+5g\theta+3f\phi'-2f'\phi-\frac{1}{Pr}\left(\frac{c_{p_w}}{c_{p_\infty}}\right)\left(\frac{T_\infty}{T_w}\right)\times\left\{\left(\frac{\theta-Y_{o,\infty}\dfrac{Q}{h_\infty}}{\tilde{c}_p}+1\right)\left[1-\xi\left(\frac{T_\infty}{T_w}\right)\left(\frac{\phi_w}{\tilde{c}_{p_w}}\right)z\right]+\xi\frac{\phi}{\tilde{c}_p}\right\}\left[\frac{N_R}{T_\infty}\frac{dq_r''}{dy}\right]=0; \quad (24)$$

and for $\eta>\eta_f$,

$$f'''-2(f')^2+3ff''+\frac{1}{\tilde{c}_p}(\theta-W_F)-2\xi(f'g'-gf'')=0, \quad (25)$$

$$g'''+5gf''+3fg'+\frac{(\phi-V_F)}{\tilde{c}_p}+(\theta-W_F)\frac{d}{d\xi}\left(\frac{1}{\tilde{c}_p}\right)=0, \quad (26)$$

$$\frac{1}{Pr}\theta'' + 3f\theta' - \frac{1}{Pr}(\xi N)\left(\frac{c_{p_w}}{c_{p_\infty}}\frac{\rho_w}{\rho_\infty}\right)\frac{1}{\tilde{\bar{c}}_p} \times [\theta - W_F]\frac{1}{T_\infty}\frac{dq_r''}{dy} - 2\xi[f'\phi - g\theta'] = 0, \quad (27)$$

$$\frac{1}{Pr}\phi'' + 5g\theta' + 3f\phi' - 2f'\phi - \frac{1}{Pr}\left(\frac{c_{p_w}}{c_{p_\infty}}\right)\left(\frac{T_\infty}{T_w}\right) \left\{\left(\frac{\theta - W_F}{\tilde{\bar{c}}_p} + 1\right)\left[1 - \xi\left(\frac{T_\infty}{T_w}\right)\left(\frac{\phi_w}{\tilde{\bar{c}}_{p_w}}\right)\right] + \xi\left(\frac{\phi - V_F}{\tilde{\bar{c}}_p}\right)\right\}\left[\frac{N_R}{T_\infty}\frac{dq_r''}{dy}\right] = 0. \quad (28)$$

With the boundary conditions:

$\eta = 0$,

$$f' = g' = 0,$$

$$f_w = \frac{4}{15}B\xi^{1/2},$$

$$g_w = -\frac{1}{10}B\xi^{-1/2},$$

$$(W_F)_w = \frac{-W_F'(\xi,0)}{Sc(3f_w + 2\xi g_w)} + \frac{Q}{h_\infty M_F(v_F'' - v_F')} + \hat{Y}_{o,\infty}\frac{Q}{h_\infty},$$

$$(W_P)_w = \frac{-W_P'(\xi,0)}{Sc(3f_w + 2\xi g_w)} + \hat{Y}_{o,\infty}\frac{Q}{h_\infty},$$

$$(V_F)_w = \frac{1}{BSc\xi^{1/2}}\left[V_F'(\xi,0) - \frac{W_F'(\xi,0)}{2\xi}\right],$$

$$(V_P)_w = \frac{1}{BSc\xi^{1/2}}\left[V_P'(\xi,0) - \frac{W_P'(\xi,0)}{2\xi}\right],$$

where $B = \frac{v_w k_w^{1/2}}{\nu_w}(N)^{1/2}$,

$$\theta_w = \frac{c_{p_w}}{c_{p_\infty}}\left(\frac{T_w}{T_\infty} - 1\right) + \hat{Y}_{o,\infty}\frac{Q}{h_\infty},$$

$$\phi_w = \left(\frac{c_{p_w}}{c_{p_\infty}}\right)\left(\frac{1}{T_\infty}\right)\left(\frac{2x}{\xi}\right)\frac{dT_w}{dx};$$

and $\eta \to \infty$,

$$f' = g' = W_F = W_P = V_F = V_P = \theta = \phi \to 0.$$

The term $d\tilde{\bar{c}}_p^{-1}/d\xi$ in equations (22) and (26) should be expressed in terms of θ or W_F, because the specific heat of the gas mixture is a function of species concentration and local temperature, i.e. $c_p = \sum_z Y_z c_p^z(T)$.

THE RADIATION MODEL

The gas radiative flux is known to be a function of the wave length, the physical length, temperature, gas concentration and the pressure. In the case of a diffusion flame, the term dq''/dy in the energy equation becomes significant. Among the five gas species in the diffusion flame, only H_2O, CO_2 and CH_4 absorb and emit thermal energy. The contribution to the total radiative flux from each gas band under non-homogeneous conditions must be evaluated individually. At 1 atm pressure, the integrated band intensity α and its band width parameter ω are major factors in the calculation of the radiative flux. On the basis of the exponential wide-band model [6] together with the scaling technique [11, 12] for non-homogeneous and non-isothermal gases, the radiative heat flux is formulated in the present study into an integral equation similar to that in [13, 15]. Here the fuel surface is taken to be black and there are no soot particles in the diffusion flame. However, it is to be noted that contrary to that in [13], the integrated band intensity, α, is treated as an integral term instead of a scaled value [12]. As suggested in [15, 16] the total band absorptance $A_{i,j}$ takes the form introduced by Tien and Lowder [10]. The complete transfer equation for 1-dim. thermal radiation is written in the following form which also includes the overlapping gas band, H_2O and CO_2 at 2.7 μm:

$$q_r''(y) = e(0) - e(\infty) + \int_0^y \frac{dT}{dy'}H_1(y', y)\,dy' + \int_y^\infty \frac{dT}{dy'}H_2(y, y')\,dy', \quad (29)$$

$$H_1(y', y) = \sum_{\substack{i,j \\ i,j \neq CO_2,\,2.7\mu}} \frac{de_{v_i}}{dT}A_{i,j}\left[\frac{3}{2}(\tau_H - \tau_H')\right] + \frac{de_{v_{2.7}}}{dT}\Gamma\left[\frac{3}{2}(\bar{\tau} - \bar{\tau}')\right]_{H_2O,\,2.7\mu} \times A_{CO_2,\,2.7\mu}\left[\frac{3}{2}(\tau_H - \tau_H')\right],$$

$$H_2(y, y') = \sum_{\substack{i,j \\ i,j = CO_2,\,2.7\mu}} \frac{de_{v_i}}{dT}A_{i,j}\left[\frac{3}{2}(\tau_H' - \tau_H)\right] + \frac{de_{v_{2.7\mu}}}{dT}\Gamma\left[\frac{3}{2}(\tau' - \tau)\right]_{H_2O,\,2.7\mu} \times A_{CO_2,\,2.7\mu}\left[\frac{3}{2}(\tau_H' - \tau_H)\right],$$

where

$$\Gamma\left[\frac{3}{2}(\tau - \tau')\right] = \exp\left[-\frac{3}{2}\int_{y'}^{y}\kappa_{v_{H_2O,\,2.7\mu}}\rho_{H_2O}\,dy''\right],$$

$$\kappa_{v_{H_2O,\,2.7\mu}} = 1212\left(\frac{\bar{T}}{300}\right)\exp\left[-0.678\left(\frac{\bar{T}}{300}\right)\right],$$

$$A_{i,j}\left[\frac{3}{2}(\tau_H - \tau_H')\right] = \bar{A}_{i,j}\left[\frac{3}{2}(\tau_H - \tau_H')\right]\bar{\omega}_{i,j}(\bar{T}),$$

$$(\tau_H - \tau_H') = \int_{y'}^{y}\left(\frac{\alpha}{\omega}\right)_{i,j}\rho_j\,dy'',$$

$$\bar{T} = \frac{1}{(y - y')}\int_{y'}^{y}T(y'')dy'',$$

and i and j indicate the radiation parameters of the ith gas band for the jth gas species.

There are altogether 11 gas bands considered in the radiation analysis. Their individual significance will be discussed in a later section. The derivative of the radiative flux dq_r''/dy is obtained by direct differentiation of equation (29), resulting in

$$\frac{dq_r''(y)}{dy} = \int_0^y \frac{dT}{dy'} G_1(y', y)\,dy' - \int_y^\infty \frac{dT}{dy'} G_2(y, y')\,dy' \quad (30)$$

where

$$G_1(y', y) = \sum_{i,j} \left[\frac{de_{v_i}}{dT}\frac{dT}{dy'}\bar{\omega}_{i,j}(\bar{T})\left\{\left[\frac{T(y)}{\bar{T}} - 1\right] \times \frac{1}{2(y-y')}\bar{A}_{i,j}(t) + \left[\frac{3}{2}\frac{\alpha_{i,j}(y)}{\omega_{i,j}(y)}\rho_i(y)\right] dA_{i,j}(t)dt\right\}\right] - \Gamma\left[\frac{3}{2}(\bar{\tau}-\bar{\tau}')\right]\frac{3}{2}\left[\bar{\kappa}_{v_{H_2O,2,7\mu}}(\bar{T})\rho_{H_2O}(y)\right],$$

$$t = \int_{y'}^{y}\left(\frac{\alpha}{\omega}\right)_{i,j} P_i\,dy'', \quad \bar{T} \frac{1}{(y-y')}\int_{y'}^{y} T(y'')\,dy'',$$

$$G_2(y, y') = \sum_{i,j}\left[\frac{de_{v_i}}{dT}\bar{\omega}_{i,j}(\bar{T}) \times \left\{\left[\frac{T(y)}{\bar{T}} - 1\right]\frac{1}{2(y'-y)}A_{i,j}(t) + \left[\frac{3}{2}\frac{\alpha_{i,j}(y)}{\omega_{i,j}(y)}\rho_i(y)\right]\frac{d\bar{A}_{i,j}(t)}{dt}\right\} - \Gamma\left[\frac{3}{2}(\bar{\tau}'-\bar{\tau})\right]\frac{3}{2}\left[\bar{\kappa}_{v_{H_2O,2,7\mu}}(\bar{T})\rho(y)\right],$$

$$t = \int_{y}^{y'}\left(\frac{\alpha}{\omega}\right)_{i,j} P_i\,dy'', \quad \bar{T} = \frac{1}{(y'-y)}\int_{y}^{y'} T(y'')\,dy''$$

The presence of dq_r''/dy in the energy equation can be either processed in the x–y or the ξ–η coordinate system, and it is basically treated as a source term with its value updated by an iteration method.

In order to examine the feasibility of using a gray-gas model for diffusion flame problems, a locally scaled Planck mean absorption coefficient can be employed in the derivative of the radiative flux as follows [17]:

$$\frac{dq_r''(y)}{dy} = \kappa_P\left\{4\sigma T^4(y) - 2\sigma\left[T_w^4 E_2(\kappa_P y) + \int_0^y T^4(x, y')E_1[\bar{\kappa}_P(y-y')]dy' + \int_y^{\cdot} T^4(x, y')E_1[\bar{\kappa}_P(y'-y)]dy'\right\},$$

$$E_2(t) \cong \frac{3}{4}\exp\left(-\frac{3}{2}t\right),$$

$$\bar{\kappa}_P(y) = \beta[Y_{H_2O}(\bar{\kappa}_P)_{H_2O} + Y_{CO_2}(\bar{\kappa}_P)_{CO_2}],$$

$$(\bar{\kappa}_P)_\alpha = \kappa_{P\alpha}(\bar{T}),$$

where β is a weighting factor.

Since the dominant radiation intensity is that due to H_2O and CO_2, the contribution to $\bar{\kappa}_P$ from CH_4 is neglected. The values of $\bar{\kappa}_P$ as a function of temperature is taken from [18].

The analytical solutions of the governing equations [(17)–(28)] are obtained by the Runge–Kutta integration scheme. The missing boundary conditions on the fuel surface, such as θ', f'', W_α' for the local similarity model and θ', ϕ', f'', g'', W_α', V_α' for the two-equation model are resolved by a shooting technique [19]. The total least square error of variables is limited to be less than 10^{-8}.

EXPERIMENTS

The experiment was performed in the Heat Transfer Laboratory of the University of Notre Dame. The test section is a 4 × 5.08 × 0.762 cm thick flat porous plate made of 58% dense nickel foametal. This porous plate is framed by four pieces of 2.54 cm thick marinite plates as shown in Fig. (2a) and then positioned in a rectangular steel frame. The success of the experiment relies greatly on the holding power of the steel frame to prevent the gas fuel leaking out of the interfaces. This whole front plate is fastened onto an aluminum base plate (12.7 × 14.29 × 1.27 cm) as shown in Fig. 2. In between there is a gasket of rubber and asbestos paper. In the base plate are twelve 0.63 cm dia. holes in an area directly behind the porous plate. Behind the base plate, another small hollowed aluminum plate is screwed onto the base plate, and fitted with three copper tubes, through which 99.95% pure methane gas is injected into the back side of the test section through the twelve holes.

The complete test section was set on an adjustable camera stand and placed in a large three-layer painted screen enclosure to minimize air circulation. The enclosure was in turn located in the test section of a Mach–Zehnder interferometer. To keep the environment of the experiment quiescent, a heavy curtain was hung around the experimental area.

The volumetric flow rate of methane gas was measured by a precision flow meter. The surface temperatures of the porous plate were measured with a 30 gauge, 0.254 mm dia. chromel–alumel thermocouple. The primary instrument in the experiment is the 15.2 cm Mach–Zehnder interferometer with a high pressure vapor light source with 0.5461 μm wavelength.

In analyzing the interferograms for the temperature profiles obtained from the fringe patterns two very important problems must be accounted for. The end effects resulting from the 3-dimensionality of the flame create a need to adopt an equivalent length scale in place of the physical width of the apparatus. The procedure used to account for this is the same as that found in [13]. The second problem involves correction for the fact that the refractive index is a function of both

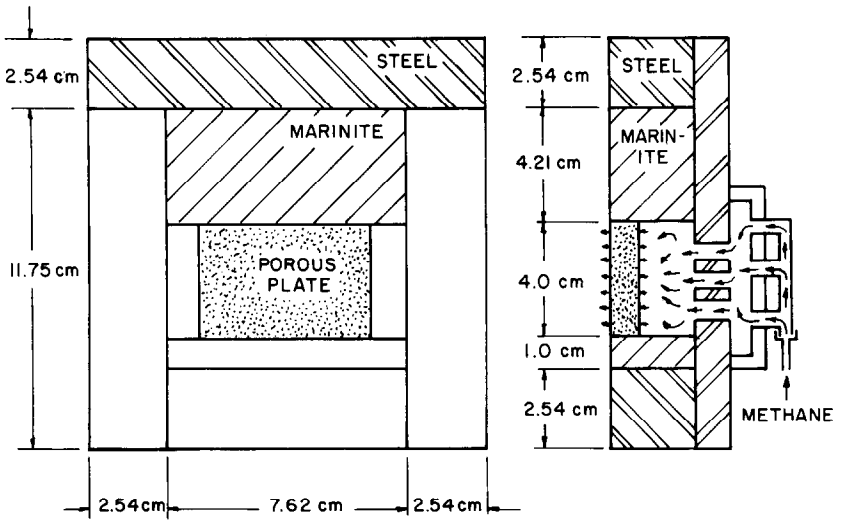

FIG. 2. Schematic drawing of methane injection burner.

temperature and species, which changes with distance up and away from the test surface. The fringe shift profiles at various vertical locations were analyzed under a microscope and then the correlation between the fringe shift number and the density was analyzed on the computer. In the present study, the measurement of gas concentrations across the boundary layer was not carried out, primarily because of the short period for measurement due to the rapid deterioration of the marinite material. However, the sensitivity of the gas concentration to the accuracy of the determination of the temperature profile is not severe. By taking the data from the experiments of Negrelli *et al.* [13], it was found that even with 10% deviation from the measured species concentrations, the resulting molar refractivity and the temperature of the gas mixture did not exceed 0.4% at the worst point, which is at the flame sheet. Based on this conclusion, the needed concentration profile for interpretating the interferograms was taken to be that of the theoretical predictions.

RESULTS AND DISCUSSION

The governing equations for the two-equation model are solved at various vertical locations along the porous surface. As discussed previously, the local similarity solution served as the initial input for the solution of the two-equation model. In order to proceed with the calculation the initial boundary conditions $W_\alpha(\xi, 0)$, $W'_\alpha(\xi, 0)$, $V_\alpha(\xi, 0)$ and $V'_\alpha(\xi, 0)$ were determined by the iteration scheme previously discusssed. The values obtained for the various locations are given in Table 1.

The methane mass rate of injection and the local temperatures for the calculations were taken from the experiments. The flow rate of the injected gas fuel is an important factor affecting the stability of the diffusion flame. When the flow rate becomes too small, thermal quenching results in an unsteady non-uniform flame. If the flow rate is too high, the flame will become unsteady and luminous, and the fringes of the interferogram are completely destroyed. It was found that the range of the flow rate to produce an extremely stable flame is very narrow, between 1400 and 1550 cc/min. All the experimental results were taken at the test run of 1500 cc/min and a typical interferogram is seen in Fig. 3. The temperature data used for comparison with the theoretical results were read between 2 and 3.4 cm from the leading edge, where the most distinguishable fringe shifts existed. Within this length of the plate the fuel surface temperature was measured in the vicinity of 750 K, while the ambient temperature was kept at 298 K.

Fringe shift data from the interferogram and complete sets of corresponding calculations were obtained at two locations on the porous plate. Figure 4 shows the profiles for the x location of 3.2 cm up the plate. Experimental and analytical profiles and species profiles are plotted as a function of distance from the surface. The vertical dashed line indicates the location of the flame sheet.

The two-equation model temperature profile shows reasonably good agreement with the data. The peak temperature in the flame and the location of the flame are seen to be predicted very accurately. Outside the flame sheet the two-equation model underpredicts the temperature. The explanation for this is found by a careful comparison of the experimental apparatus with the prescribed boundary conditions. Of course, with a blowing of fuel at the surface of the porous plate the thickness of the entire flame region is increased and the boundary layer assumption tends to break down. Also, as mentioned previously, the porous plate was surrounded by marinite plates and a steel frame. During the combustion process the surrounding materials are heated, even below the leading edge of the porous plate. Measurement indicates that the temperature of the marinite plate below the porous

Table 1. Surface boundary conditions necessary for local similarity and two-equation calculations

ξ	$W_F(0,\xi)_{\text{loc sim}}$	$W'_F(0,\xi)_{\text{loc sim}}$	$W_F(0,\xi)_{\text{2-Eqn}}$	$W'_F(0,\xi)_{\text{2-Eqn}}$	$V_F(0,\xi)_{\text{2-Eqn}}$	$V'_F(0,\xi)_{\text{2-Eqn}}$
0.57738	−24.008	18.947	−22.24	19.209	−13.78	14.827
0.60742	−24.512	19.376	−22.70	19.636	−13.35	14.324
0.63604	−24.978	19.763	−23.11	20.022	−12.99	13.899
0.66343	−25.414	20.122	−23.50	20.367	−12.68	13.606
0.68973	−25.824	20.458	−23.87	20.741	−12.40	13.218
0.71506	−26.212	20.773	−24.22	21.069	−12.14	12.917
0.73953	−26.579	21.071	−24.55	21.378	−11.91	12.648
0.76321	−26.927	21.353	−24.86	21.665	−11.69	12.391
0.78618	−27.259	21.621	−25.16	21.945	−11.49	12.168
0.80850	−27.575	21.877	−25.45	22.212	−11.30	11.955
0.83022	−27.874	22.121	−25.73	22.473	−11.13	11.753
0.85138	−28.354	22.354	−25.99	22.712	−10.96	11.563
0.87203	−28.447	22.579	−26.24	22.942	−10.81	11.393
0.89221	−28.716	22.794	−26.49	23.171	−10.66	11.225
0.91193	−28.976	23.002	−26.73	23.389	−10.52	11.067
0.93124	−29.227	23.202	−26.95	23.592	−10.39	10.920
0.95016	−29.472	23.395	−27.18	23.802	−10.27	10.78
0.96871	−29.707	23.583	−27.37	23.973	−10.14	10.637
0.98691	−29.938	23.763	−27.58	24.163	−10.02	10.501
1.0048	−30.161	23.939	−27.79	24.352	− 9.910	10.266
1.0223	−30.377	24.109	−27.98	24.524	− 9.805	10.266
1.0396	−30.587	24.274	−28.18	24.702	− 9.705	10.151
1.0566	−30.788	24.436	−28.36	24.863	− 9.608	10.040
1.0733	−30.987	24.592	−28.54	25.027	− 9.515	9.943
1.0897	−31.182	24.746	−28.72	25.190	− 9.425	9.840
1.1059	−31.371	24.894	−28.90	25.351	− 9.339	9.750
1.1219	−31.558	25.040	−29.07	25.503	− 9.255	9.653
1.1532	−31.916	25.319	−29.40	25.798	− 9.096	9.478
1.1837	−32.258	25.587	−29.71	26.073	− 8.947	9.314

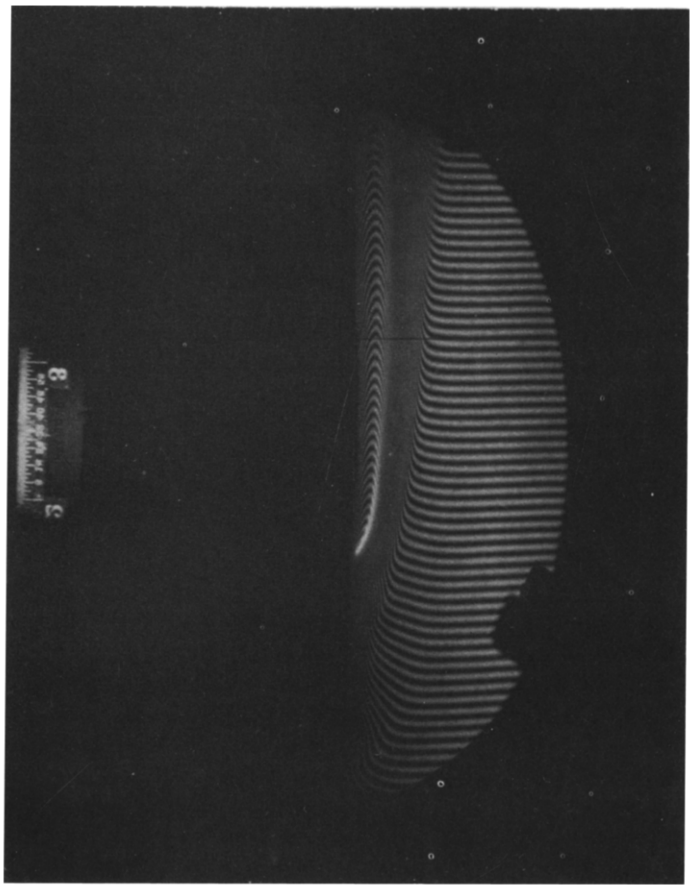

FIG. 3. Interferogram of methane flame adjacent to vertical porous plate burner.

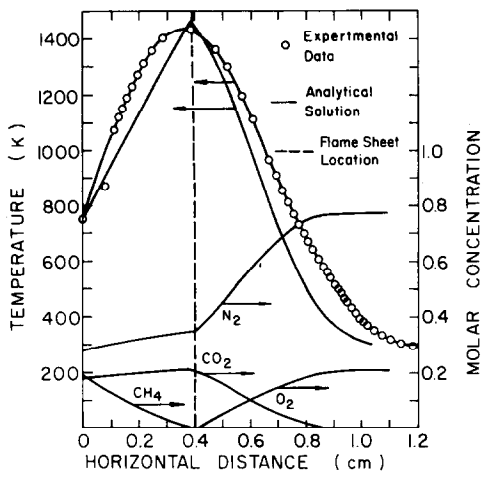

FIG. 4. Analytical temperature and species profile predictions compared with experimental data at a vertical height of 3.2 cm.

plate varies from 380 to 470 K. Consequently, the thermal boundary layer begins to develop far below the porous plate. The thickened boundary can also be examined from the interferogram in Fig. 3. It is seen that the boundary layer actually grows beginning at the bottom of the steel frame. Although the two-equation model solution underestimates the boundary layer thickness, the temperature gradients at the fuel surface, the location of flame sheet and the peak flame temperatures are all predicted with fairly good accuracy.

It should be pointed out also that the theory assumes an infinitely thin flame sheet which results in the pointed profiles. Obviously, the experimental data indicate a finite thickness combustion region as evidenced by the rounded profiles in the region of the flame and by actual observation of the flames. This would also tend to increase the experimental boundary layer thickness compared to the theoretical prediction. A finite reaction rate model instead of the flame sheet model should take care of this problem.

As prescribed by the flame sheet model the methane concentration is seen to be zero outside the flame and the oxygen concentration is zero inside the flame. As observed in the study by Negrelli *et al.* [13], the nitrogen concentration drops steeply from outside the flame up to the flame. Between the flame front and the surface it drops slowly to a value of just under 0.3. At the porous surface the concentration of the methane is not 100%. This, as observed by others [9, 13], is due to the fact that the nitrogen, carbon dioxide and water vapor all diffuse toward the wall. Somewhere within the porous surface concentrations of these species do go to zero and the gas is pure methane.

Figure 5 shows the experimental and analytical temperature profiles for $x = 2.4$ cm. The peak flame temperature is higher at this location and the sheet is located closer to the surface than at 3.2 cm. The peak temperatures for the experiment and the analysis are in good agreement as is the location of the flame. In the outer region the analysis underpredicts the temperature, but this in light of the previous discussion, is expected.

The sensitivity of the surface injection rate on the results was investigated. The higher the surface injection speed, the higher the maximum calculated flame temperature will be. The maximum flame temperature, according to the analytical model and as shown in Fig. 6, approaches an asymptotic value of nearly 1680 K. In an experiment this high flame temperature could not be possible in view of the instability of the laminar diffusion flame and finite reaction rates. At the lower end of the injection rates, quenching of the flame occurs, and the flame sheet becomes unstable.

In the studies of radiation–convection interactions in flow along a vertical plate by Hasegawa *et al.* [20] and combustion in laminar boundary layers by Kikkawa *et al.* [21], the significance of variable physical properties to the temperature profiles has been emphasized. The effect of specific heat was carefully examined in the present study and was found to have a very significant effect on the predicted temperature profiles and therefore the heat transfer. In one calculation at $X = 0.8$ the specific heat was maintained constant at 0.25, and then in a second calculation it was evaluated locally as a function of the temperature and species concentration. The peak temperature was 400 K hotter, the temperature gradient at the wall was doubled, and the boundary layer was thicker for the constant property solution. Variation in physical properties should definitely be accounted for whenever possible.

Unlike the specific heat, radiation has its influence in

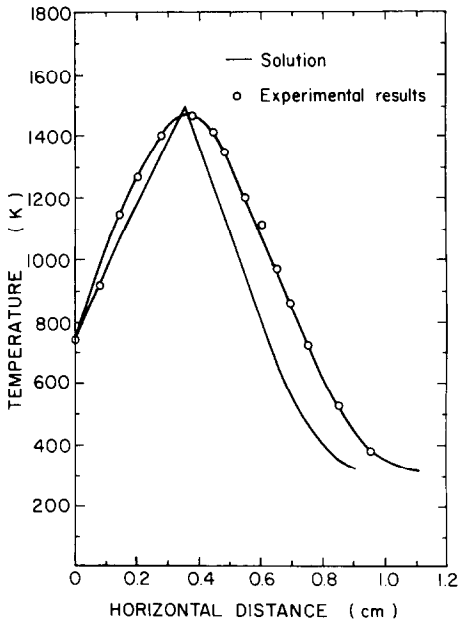

FIG. 5. Comparison of temperature profiles in flame adjacent to the burner at a vertical height of 2.4 cm.

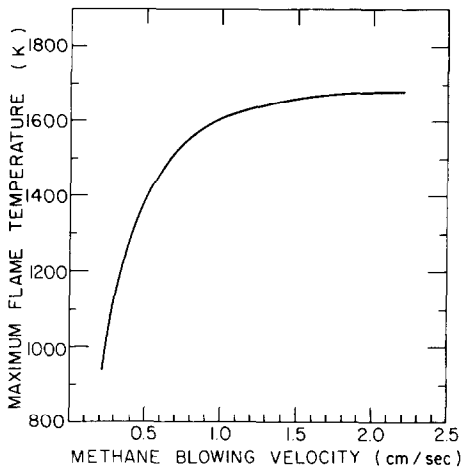

FIG. 6. Predicted peak flame temperature as a function of methane injection rate, at a vertical height of 3.2 cm.

two different aspects. First, the peak temperature is reduced by approx. 100 K at $X = 3.2$ cm, and the location of the flame sheet was slightly shifted due to the change of $W_F(\xi, 0)$ on the fuel surface. Secondly, the radiation reduces the flame temperature inside the flame sheet and increases the boundary layer thickness, which has also been observed by Negrelli *et al.* [13].

In order to examine the importance of individual gas bands, the radiative flux for each band and its percentage contribution to the total radiative flux are listed in Table 2. It is obvious that the combined contribution from CO_2 4.3 μm, H_2O 2.7 μm and 6.3 μm bands is over 85% of the total gas radiation, and this is also true at other vertical locations on the porous plate. Consequently, for a methane diffusion flame a good estimate of the gas radiation can be achieved by considering only three strong bands, instead of the entire 11 bands. This computation time could be shortened by as much as 65%. This observation is in agreement with the findings of [13].

The assumption of a gray gas would simplify the calculation of the radiation flux and reduce CPU time. In this study the gray gas approximation was attempted using a locally scaled Planck mean absorption coefficient [22]. It has been recognized that the Planck mean absorption coefficient is only a wave length averaged quantity and cannot be treated as a constant in the nonhomogeneous gas volume. Therefore, the $\bar{\kappa}_p$ value should be determined as a function of temperature and species concentration. From several different numerical experiments, it was found that the local $\bar{\kappa}_p$ ought to be a scaled value as it was in the wide-band model, i.e.

$$\bar{\kappa}_p = \sum_i Y_i \kappa_{pi}(\bar{T}).$$

Due to some uncertainties in the $\bar{\kappa}_p$ data for pure gases by Tien [23], the final $\bar{\kappa}_p$ used in the diffusion flame was modified by a factor which is varied from 0.1 to 1.0. Generally, a value of 0.4 had the best match to the dq_r''/dy profile of the wide-band model. During the current study, the temperature dependence of the $\bar{\kappa}_p$ value has also been approximated by (a) a constant wall reference value, (b) a global average gas volume temperature, (c) a local gas temperature. They all matched at a specific location of x with the adjustment of the factor, but none of them were able to match the dq_r''/dy and the temperature profiles at any other x locations.

Finally, the question of the adequacy of the local similarity solution compared to the two-equation model must be addressed. The local similarity solution is much simpler and requires far less computer time. Figure 7 compares the temperature profiles at $X = 3.2$ cm for the local similarity model, the two-equation model and the experiment. The region where agreement is good when compared to experiment is in the outer regions. As discussed previously this is not necessarily a virtue since from a heat transfer point of view the region close to the wall is the most important. The two-equation model is therefore preferred over the local similarity model.

CONCLUSION

This analytical and experimental study deals with

Table 2. The contribution of individual gas band to the total gaseous radiation heat flux at the fuel surface $X = 2.94$ cm

Gas species	Band (μm)	Radiative heat flux (W/cm^2)	Contribution percentage (%)
H_2O	2.7	−4.636 E-02	13.6
H_2O	6.3	−4.98 E-02	14.6
H_2O	1.38	−0.261 E-02	0.766
H_2O	1.87	−0.674 E-02	1.98
CO_2	2.7	−1.572 E-02	4.644
CO_2	4.3	−1.956 E-01	57.41
CO_2	15.0	−7.55 E-03	2.22
CO_2	9.4	−1.27 E-04	0.0373
CO_2	10.4	−1.09 E-04	0.0319
CH_4	3.3	−1.198 E-02	3.518
CH_4	7.6	−3.95 E-03	1.161

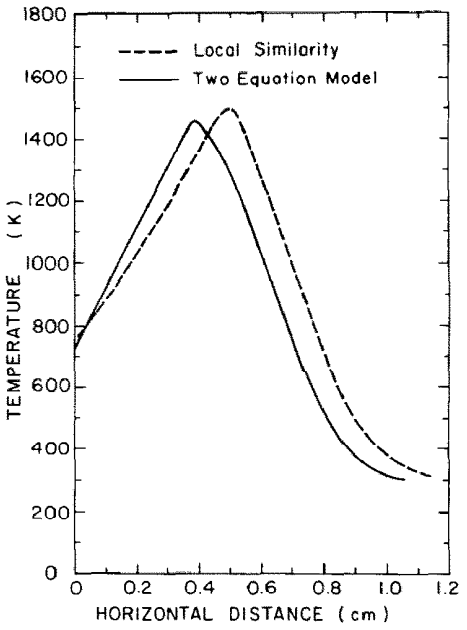

FIG. 7. Comparison of local similarity and local non-similarity temperature profiles at a vertical height of 3.2 cm.

the phenomenon of a diffusion flame boundary layer flow on a vertical plate with methane injection. The governing conservation equations with an exponential wide-band radiation model are solved by the local non-similarity method, and results are compared with the experimental data obtained by a Mach–Zehnder interferometer.

The analytical results agree satisfactorily with the corresponding experimental data in terms of the temperature variations within the flame, the peak temperature resulting from the combustion process and the fuel surface heat transfer, but underestimates the overall boundary layer thickness. However, it is felt that this latter discrepancy is primarily a result of the development of the thermal boundary layer below the porous plate leading edge in the experimental situation.

This study provides further evidence of the velocity of the exponential wide-band radiation model for predicting the behaviour of non-homogeneous and non-isothermal gases at atmospheric pressures. Among the 11 gas bands considered in the diffusion flame, only three of them, CO_2 4.3 μm, H_2O 2.7 μm and 6.3 μm bands, are dominant, and their combined contribution in radiative heat flux exceeds 85% of the total gas radiation. The thermal radiation effect from the diffusion flame is to reduce the peak flame temperature and also to increase the boundary layer thickness.

The locally scaled Planck mean absorption coefficient has been shown to predict with good accuracy the derivatives of the radiative heat flux in the present problem when compared to that of the exponential wide-band model. But the coefficient must be considered to be a function of the specific location and not for the entire flame.

The variable physical property effect must be accounted for in any diffusion flame study. It is found in the present study that constant specific heats give unsatisfactory results regarding the flame structure and temperatures.

Acknowledgements—The authors gratefully acknowledge the support given by the National Science Foundation under Grant No. ENG76-81904 and by the Computing Center of the University of Notre Dame.

REFERENCES

1. R. D. Cess, The Interaction of Thermal Radiation with Free Convention Heat Transfer, *Int. J. Heat Mass Transfer* **8**, 1269–1277 (1966).
2. J. L. Novotny, Radiation Interaction in Nongray Boundary Layers, *Int. J. Heat Mass Transfer* **11**, 1823–1826 (1968).
3. W. P. Schimmel, J. L. Novotny and F. Olsofka, Interferometric Study of Radiation–Conduction Interaction, *Proc. 4th Int. Heat Trans. Conf.*, Paper R21, Elsevier Amsterdam (1970).
4. J. C. Bratis and J. L. Novotny, Radiation–Convection Interaction in Real Cases, *AIAA Progress in Astronautics and Aeronautics* **31**, 329–348 (1973).
5. T. Audunson and B. Gebhart, An Experimental and Analytical Study of Natural Convection with Appreciable Thermal Radiation Effects, *J. Fluid Mech.* **52**, 57–95 (1972).
6. D. K. Edwards and W. A. Menard, Comparison of Models for Correlation of Total Band Absorption, *Appl. Optics* **3**, 621–625 (1964).
7. J. S. Kim, J. deRis and F. W. Kroesser, Laminar Free-Convective Burning of Fuel Surfaces, *13th Symposium (International) on Combustion, The Combustion Institute* 949–961 (1971).
8. E. G. Groff and G. M. Faeth, Laminar Combustion of Vertical Free-Standing Fuel Surface, *Combustion and Flame* **32**, 139–150 (1978).
9. S. Abdel-Khalik, T. Tamara and M. M. El-Wakil, An Experimental and Analytical Determination of Heat and Mass Transfer in a Diffusion Flame, *Proceedings 1973 International Center for Heat and Mass Transfer Seminar—Heat Transfer from Flames*, Scripta Publishing (1974).
10. C. L. Tien and J. E. Lowder, A Correlation for the Total Band Absorptance of Radiating Gases, *Int. J. Heat Mass Transfer* **9**, 698–701 (1966).
11. D. K. Edwards and S. J. Morizumi, Scaling of Vibration–Rotation Band Parameters for Non-homogeneous Gas Radiation, *J. Quant. Spectros. Radiat Transfer* **10**, 175–178 (1970).
12. J. D. Felske and C. L. Tien, Infrared Radiation from Nonhomogeneous Gas Mixture Having Overlapping Bands, *J. Quant. Spectros. Radiat. Transfer* **14**, 35–48 (1974).
13. D. E. Negrelli, J. R. Lloyd and J. L. Novotny, A Theoretical and Experimental Study of Radiation–Convection Interaction in a Diffusion Flame, *J. Heat Transfer* **99**, 212–220 (1977).
14. E. M. Sparrow and H. S. Yu, Local Nonsimilarity Thermal Boundary Layer Solutions, *J. Heat Transfer, Trans. ASME, Ser. C* **93**, 328–334 (1971).
15. J. L. Novotny, Formulation of One-Dimensional Radiative Flux for Non-homogeneous Non-gray Gases and Soot, Technical Report TR-37191-74-1, Department of Aerospace and Mechanical Engineering, University of Notre Dame (1974).
16. J. D. Bankston, J. R. Lloyd and J. L. Novotny, Radiation–Convection Interaction in an

Absorbing–Emitting Liquid in Natural Convection Boundary Layer Flow, *J. Heat Transfer* **99C**, 125–127 (1977).
17. R. Siegel and J. R. Howell, *Thermal Radiation Transfer*, McGraw–Hill, New York (1972).
18. E. M. Sparrow and R. D. Cess, *Radiation Heat Transfer*. Brooks/Cole, Belmont, California, (Revised Edition, 1970).
19. W. P. Nachtscheim and P. Swigert, Satisfaction of the Asymptotic Boundary Conditions in the Numerical Solutions of Boundary Layer Equations, *Developments in Mechanics* **3**, (2), 361–371 (1965).
20. S. Hasegawa, R. Echigo and K. Fukuda Analytical and Experimental Studies on Simultaneous Radiative and Free Convection Heat Transfer Along a Vertical Plate, *Proc. Japan Soc. mech. Engrs* **38**, (315), 2873–2882 (1972).
21. S. Kikkawa and K. Yoshikawa, Theoretical Investigation on Laminar Boundary Layer with Combustion on a Flat Plate, *Int. J. Heat Mass Transfer* **16**, 1215–1229 (1973).

ETUDE D'UNE FLAMME LAMINAIRE DE DIFFUSION ADJACENTE A UNE PLAQUE PLANE VERTICALE

Résumé—On étudie analytiquement et expérimentalement une flamme de diffusion de méthane dans la région adjacente à une plaque plane verticale. Les équations appropriées de la couche limite, incluant le rayonnement thermique monodimensionnel non-gris et non-homogène formulé sur la base du modèle exponontiel de bande, sont résolues par la méthode de non-similitude locale pour déterminer les profils de concentration des espèces, de vitesse et de température dans la couche limite de la flamme. On montre que les propriétés physiques variables du mélange de gaz ont des effets importants sur la température et la structure de la flamme. La forme de la flamme et la distribution de température dans la couche limite ont été déterminées par interférométrie Mach–Zehnder pour vérifier les résultats théoriques. Le pic de température, sa position et le profil de température dans la flamme sont correctement prédits par les solutions à deux équations qui, par contre, sous-estiment les épaisseurs de couche limite. A partir de ces résultats, on explore la possibilité d'un modèle de rayonnement de gaz gris.

UNTERSUCHUNG EINER LAMINAREN DIFFUSIONSFLAMME AN DER VERTIKALEN EBENEN PLATTE EINES BRENNERS

Zusammenfassung—Es wird eine analytische und experimentelle Untersuchung einer Methandiffusionsflamme an der senkrechten Platte eines Brenners durchgeführt. Die entsprechenden Grenzschichtgleichungen, welche die eindimensionale nichtgraue, nichthomogene thermische Strahlung berücksichtigen und auf der Basis des exponentiellen Breitbandmodells formuliert wurden, werden nach dem Verfahren der örtlichen Nichtähnlihkeit gelöst, um die Gaszusammensetzung und die laminaren Geschwindigkeits- und die Temperaturprofile im Innern der Diffusionsflammengrenzschicht zu bestimmen. Es wird gezeigt, daß verschiedene physikalische Eigenschaften der Gasmischung starke Auswirkungen auf Flammentemperatur und -struktur haben. Die Diffusionsflammenform und Temperaturverteilung in der Grenzschicht wurden mit einem Mach–Zehnder-Interferometer gemessen, um die theoretischen Ergebnisse zu überprüfen. Die maximale Flammentemperatur, ihre Position und das Temperaturprofil im Innern der Flamme werden durch die zwei Gleichungen der Lösung genau bestimmt, wobei sich die Grenzschichtdicke jedoch zu gering ergibt. Auf der Grundlage dieser Ergebnisse wird auch die Brauchbarkeit eines Modells der grauen Gasstrahlung untersucht.

ИССЛЕДОВАНИЕ ЛАМИНАРНОГО ДИФФУЗИОННОГО ПЛАМЕНИ У ВЕРТИКАЛЬНОЙ ПЛОСКОПЛАСТИНЧАТОЙ ГОРЕЛКИ

Аннотация — Проведено аналитическое и экспериментальное исследование метанового диффузионного пламени в зоне, прилегающей к вертикальной плоскопластинчатой горелке. Для определения состава газа, ламинарной скорости и профилей температур в пограничном слое пламени методом локальной неавтомодельности решаются соответствующие уравнения пограничного слоя с учётом одномерного несерого неоднородного теплового излучения, полученного на основе экспоненциальной модели. Показано, что переменные физические характеристики газовой смеси оказывают большое влияние на температуру и структуру пламен. Форма диффузионного пламени и распределение температур в пограничном слое измерялись также с помощью интерферометра Маха–Цендера с целью проверки теоретических результатов. Максимальная температура пламени, её местоположение и профиль температур в плоскости пламени точно рассчитываются решением двух уравнений, которые, однако, дают заниженные значения толщины пограничного слоя. На основе полученных результатов исследуется справедливость модели излучения серого газа.